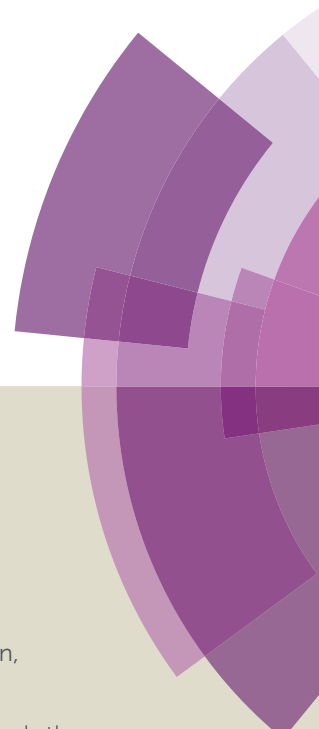


Journal of Materials Chemistry A

Accepted Manuscript



This article can be cited before page numbers have been issued, to do this please use: J. Gao, A. Martin, J. Yatvin, E. White and J. Locklin, *J. Mater. Chem. A*, 2016, DOI: 10.1039/C6TA03222B.



This is an *Accepted Manuscript*, which has been through the Royal Society of Chemistry peer review process and has been accepted for publication.

Accepted Manuscripts are published online shortly after acceptance, before technical editing, formatting and proof reading. Using this free service, authors can make their results available to the community, in citable form, before we publish the edited article. We will replace this *Accepted Manuscript* with the edited and formatted *Advance Article* as soon as it is available.

You can find more information about *Accepted Manuscripts* in the [Information for Authors](#).

Please note that technical editing may introduce minor changes to the text and/or graphics, which may alter content. The journal's standard [Terms & Conditions](#) and the [Ethical guidelines](#) still apply. In no event shall the Royal Society of Chemistry be held responsible for any errors or omissions in this *Accepted Manuscript* or any consequences arising from the use of any information it contains.



Journal Name

ARTICLE

Permanently Grafted Icephobic Nanocomposites with High Abrasion Resistance

Jing Gao, Andrew Martin, Jeremy Yatvin, Evan White and Jason Locklin*

Received 00th January 20xx,
Accepted 00th January 20xx

DOI: 10.1039/x0xx00000x

www.rsc.org/

In this work, a series of copolymer/silica nanocomposites are investigated that exhibit excellent anti-icing behavior and can be covalently grafted to any substrate containing C-H bonds with high durability. The copolymers of interest consist of pendant benzophenone, hexafluorobutyl, and a variety of other comonomers that, under mild UV irradiation, can be covalently grafted on a variety of substrates and generate a densely cross-linked network of polymer and well-dispersed nanoparticles. The robustness of thin films was compared in a series of terpolymers with different acrylic comonomer content. Thin films prepared with tert-butyl ester side groups had less backbone chain scission and, therefore, a greater extent of cross-linking than films prepared with n-butyl ester side groups. The *iso*-butyl acrylate comonomer promotes photoreaction efficiency in terms of kinetic rate and network robustness, leading to films that can sustain high shear forces and abrasion. The anti-icing capability of the composite was investigated using the impact of supercooled water on different substrates. The composite maintains its icephobicity after modified Taber testing with multiple abrasion cycles using a 300 g load, which demonstrates excellent mechanical resistance. In addition, this study has led to rational design rules for copolymers that maximize permanent attachment of different surface functionalities in terms of both grafting density and reaction kinetics.

1. Introduction

Ice accumulation on surfaces is problematic in daily life as it can cause breakage of power transmission lines, freezing on roads, and, as any homeowner can attest, buildup of ice inside domestic freezers.¹⁻³ It also raises potential issues in industrial applications such as disturbing the aerodynamics of aircraft wings and wind turbines, resulting in increased maintenance and repair costs every year.^{4, 5} The mechanism of ice formation under subzero conditions and the design of ice-repellent coatings have been areas of intense study for decades.⁶⁻¹⁰ Such coatings are expected to either minimize ice adhesion¹¹⁻¹⁴ or delay ice formation on surfaces.^{2, 8, 15, 16} Superhydrophobic surfaces, which are characterized by a high water contact angle (CA) and low water contact hysteresis (CAH), have been observed to exhibit anti-icing characteristics.^{11-13, 17, 18} Due to the small contact area between the freezing droplet and the rough surface, an air layer is formed at the interface, which reduces the ice-solid interaction. Two approaches have been utilized to fabricate anti-icing surfaces with micro/nanoscale roughness: (1) patterning substrates such as

silicon¹⁵ or metal^{13, 16, 19, 20} with ordered nano-scale features by etching or photolithography,⁷ followed by a top-coat of a fluorinated self assembled monolayer (SAM) or polymer; or (2) depositing inorganic nanoparticles (Ag, ZnO, TiO₂, etc.) directly onto surfaces,^{2, 10-12} which is likely a more feasible and scalable process for large scale application. The drawback, however, is that superhydrophobic surfaces are very fragile due to the susceptibility of the micro- or nanoscale features to mechanical abrasion or environmental conditions such as wind and rain. Superhydrophobic coatings that are attached to the surface via non-covalent interactions, such as van der Waals forces, electrostatic interactions, or hydrophobic interactions, are limited in widespread applications in harsh environments, where delamination, desorption, and/or dewetting may occur to the coating.^{21, 22}

Benzophenone (BP) photochemistry has been thoroughly studied and widely used as a photoactive tethering reagent to functionalize a wide variety of materials.²³⁻²⁷ The extensive use of BP can be attributed to the following advantages: (1) The BP moiety attaches to C-H bonds in a wide range of chemical environments, including commercial plastics and fabrics;²⁸⁻³² (2) BP can be manipulated in ambient atmosphere and activated with mild UV light (345-365 nm), which avoids oxidative damage to many materials;²⁴ and (3) BP is both thermally and chemically more stable and synthetically more versatile than most other tethering functionality, such as sulfonyl azides,³³ diazo esters,³⁴

Department of Chemistry, College of Engineering, and the Center for Nanoscale Science and Engineering, University of Georgia, Athens, Georgia, 30602, United States
E-mail: jlocklin@uga.edu

Electronic Supplementary Information (ESI) available: DSC of two terpolymers (Fig. S1), DLS of nanoparticles (Fig. S2), mathematic derivation of *f* and calculation of the value under our experimental condition, and videos of icing experiments (Movie S1 and S2). See DOI: 10.1039/x0xx00000x

aryl azides,³⁵ and diazirines.^{36, 37} Under irradiation, BP absorbs photons, resulting in the promotion of an electron from n-orbital of the carbonyl oxygen to the π^* -orbital and the formation of biradicaloid triplet state. The electron-deficient oxygen abstracts a hydrogen atom from a C-H group in close proximity, followed by the combination of two carbon radicals and the generation of a new C-C bond. This photochemistry has been used to permanently attach polymer films to a broad selection of C-H containing surfaces in many different applications, such as microfluidic devices,^{38, 39} biosensing,^{40, 41} antimicrobial coatings,³⁰ patterned sheets,^{42, 43} and organic semiconductors.⁴⁴

In this article, we describe a robust anti-icing composite that consists of well-dispersed silica nanoparticles within a cross-linked, fluorinated polymer network. The surface attachment of the composite was readily achieved by UV-initiated cross-linking between BP moieties and surface-bound C-H groups. The composite demonstrated impressive anti-icing capabilities due to its fluorinated hierarchical micro/nano-scale surface structure. The composite also resisted relatively harsh mechanical stress, which is attributed to the dense covalent network between the copolymer and nanoparticles, as well as the substrate surface. To the best of our knowledge, this is the first demonstration of the covalent immobilization of hierarchical anti-icing coatings onto surface that can withstand high abrasive forces.

2. Experimental Section

2.1 Materials

Triphenylphosphine, iodomethane, potassium *tert*-butoxide, 2,2'-azobis(2-methylpropionitrile) (AIBN), 2,2,3,4,4,4-hexafluorobutyl methacrylate, and n-butyl acrylate (nBA) were obtained from Alfa Aesar. 4-Bromobenzaldehyde, benzonitrile, and isobutyltrichlorosilane were purchased from TCI. Tetraethoxysilane was obtained from UTC and magnesium turnings were obtained from Eastman Organic. Cetyltrimethylammonium bromide was purchased from Acros Organic and isobutyl acrylate (iBA) from Sigma-Aldrich. Inhibitor was removed from the corresponding monomers by passing through a neutral aluminum column. Silicon wafers with native oxide were used as substrates. Unless otherwise noted, all compounds were used as received.

2.2 Instrumental Methods

UV-vis spectroscopy was performed on a Cary Bio spectrophotometer (Varian). The UV light sources were a Compact UV lamp (UVP) and FB-UVXL-1000 UV Crosslinker (Fisher Scientific) with bulbs of wavelength at 254 nm for small (1 × 2 cm) and large (3.6 × 4.2 cm) substrates, respectively. The substrates were held a certain distance from the light source during irradiation to obtain power of 7.5 mW cm⁻². Surface topography was analyzed with a FEI Inspec F FEG scanning electron microscopy at 20 keV. Infrared spectroscopy studies of polymer coated films were carried out using a Thermo-Nicolet model 6700 spectrometer equipped with a variable angle grazing angle attenuated total reflection (GATR-ATR) accessory (Harrick Scientific). Water contact angles were

measured using a DSA 100 drop shape analysis system (KRÜSS) with a computer-controlled liquid dispenser. Water droplets with volume of 1 μ L were used to measure the static contact angle. The advancing and receding contact angles were measured by expanding and retracting the water droplet on the substrate. The glass transition temperature (T_g) of copolymer was measured by using a differential scanning calorimeter DSC 823^e (Mettler Toledo). Data was stored and manipulated using the software STARe DB V9.20 (Mettler Toledo). Samples were scanned from -60 °C to 150 °C at a rate of 10 °C/min. Four heating and cooling cycles were conducted to minimize sample history. Nanoparticle sizing was determined using a Zetasizer Nano Series (Malvern) with dynamic light scattering (DLS).

2.3 Synthesis

Methyltriphenylphosphonium iodide

Triphenyl phosphine (12 g, 45.75 mmol), iodomethane (8.44 g, 59.8 mmol) and toluene (100 mL) were stirred at room temperature for 16 h under a nitrogen atmosphere. The reaction mixture was filtered and a pure white solid was collected. The solid was washed with diethyl ether and air-dried. Yield: 17.17 g (93%). ¹H NMR (500 MHz, CDCl₃, δ): 7.84-7.67 (m, 15H, Ar H), 3.25 (d, J = 13.3 Hz, 3H; CH₃).

4-Bromostyrene

Methyltriphenylphosphonium iodide (10.66 g, 26.4 mmol) was suspended in tetrahydrofuran (15 mL) and cooled to 0 °C in a three-neck round-bottom flask. Potassium *tert*-butoxide (3.23 g, 28.8 mmol) was dissolved in THF (10 mL) and added drop-wise to the round-bottom flask. The reaction mixture was stirred at 0 °C for 20 min and at room temperature for 10 min. 4-Bromobenzyldeheyde (4.44 g, 24.0 mmol) was dissolved in THF (10 mL) and added to the flask. The reaction was stirred at room temperature overnight. The solvent was removed under reduced pressure. The solid mixture was taken up in diethyl ether, and washed with water and brine, then dried over magnesium sulfate. The solvent was removed with a rotary evaporator. The crude product was purified on a silica gel column using a hexane:ethyl acetate (4:1) eluent. Yield: 3.97 g (90%). ¹H NMR (500 MHz, CDCl₃, δ): 7.44 (d, J = 8.8 Hz, 2H, Ar H), 7.27 (d, J = 8.2 Hz, 2H, Ar H), 6.65 (dd, J = 11.1 Hz, 1H; CH), 5.74 (d, J = 17.6 Hz, 1H; CH₂) 5.28 (d, J = 11.1 Hz, 1H; CH₂). ¹³C NMR (300 MHz, CDCl₃, δ): 136.61, 135.94, 132.27, 128.21, 125.98, 116.54.

4-Vinylbenzophenone (4VBP)

Magnesium turnings (0.65 g, 26.6 mmol) and a flake of iodine were dissolved in dry THF (5 mL) in a three-neck round-bottom flask under nitrogen atmosphere at 0 °C. 4-Bromostyrene (4.48 g, 24.5 mmol) was dissolved in anhydrous THF (5 mL) and added to the flask drop-wise from an additional funnel. The reaction mixture was stirred overnight at room temperature. A catalytic amount of copper (I) bromide and benzonitrile (2.27 g, 22.0 mmol) were added by syringe, and the reaction was stirred for 16 h. Sulfuric acid (15 mL, 15% V/V) was added to quench the reaction, followed by extraction with diethyl ether (50 mL). The organic

layer was washed with water and brine, dried over magnesium sulfate and concentrated with a rotary evaporator. The crude product was purified by column chromatography (hexane:ethyl acetate, 4:1). Yield: 2.23 g (49%). ^1H NMR (500 MHz, CDCl_3 , δ): 7.81 (d, $J = 7.6$ Hz, 2H, Ar H), 7.80 (d, $J = 8.4$ Hz, 2H, Ar H), 7.59 (t, $J = 7.6$ Hz, 1H, Ar H), 7.51 (d, $J = 8.3$ Hz, 2H, Ar H), 7.49 (t, $J = 7.8$ Hz, 2H, Ar H), 6.79 (dd, $J = 10.8$ Hz, 1H; CH), 5.90 (d, $J = 17.6$ Hz, 1H; CH_2), 5.41 (d, $J = 11.2$ Hz, 1H; CH_2). ^{13}C NMR (300 MHz, CDCl_3 , δ): 116.59, 128.27, 129.09, 129.92, 130.53, 132.31, 135.98, 136.65, 137.72, 141.53, 196.11.

Terpolymer

The polymer was synthesized by free radical polymerization of vinyl benzophenone (0.16 g, 0.79 mmol), hexafluorobutyl methacrylate (1.18 g, 4.72 mmol), and n-butyl or isobutyl acrylate (0.10 g, 0.79 mmol) in toluene (3 mL) with AIBN (0.0038 g, 0.0024 mmol) as the initiator in a Schlenk flask under nitrogen atmosphere. The degassed mixture was stirred at 65 °C for 16 h. The resulting polymer was precipitated in cold ethanol, filtered, and dried under vacuum. Yield: 0.31 g (67%). ^1H NMR (500 MHz, CDCl_3 , δ): 7.73 (bs, 4H); 7.60 (bs, 1H); 7.48 (bs, 2H); 7.14 (bs, 2H); 4.91 (bs, 6H); 4.34 (bs, 12H); 2.62 (bs, 1H), 1.89 (bs, 19H); 1.48 (bs, 2H); 1.26 (bs, 2H); 1.01 (bs, 6H) 0.937(bs, 10H); 0.72 (bs, 4H). The number average molecular weight (M_n) of two copolymers was ~ 137 kDa. \bar{D} of the copolymers that contains n-butyl and isobutyl acrylate were 1.9 and 2.0, respectively.

Surface Modified Silica Nanoparticle

An ammonia solution (10.8 g, 29% w/w) was added to deionized water (442 mL) and heated to 50 °C, followed by addition of cetyltrimethyl ammonium bromide (0.279 g) with rapid stirring. The solution was cooled to room temperature and tetraethoxysilane (1.394 mL) was added. The solution was stirred vigorously for 2 h. The water was removed by centrifugation and the white solid was dried in a vacuum oven at 60 °C for 16 h. Yield: 0.40 g. The silica nanoparticles were suspended in toluene (40 mL). Isobutyltrichlorosilane (7.662 g) was then added to the suspension and stirred rapidly for 16 h. The resulting suspension was centrifuged and supernatant was discarded. The solid was washed by resuspending in THF (30 mL), vortexing and centrifugation. This process was repeated three times. The white solid was dried in a vacuum oven overnight.

Preparation of Surface-Bound Terpolymer-Nanoparticle Composite

A silicon wafer (3.6 x 4.2 cm) was pre-treated with a self-assembled monolayer (SAM) of isobutyltrichlorosilane (iBTS) using solution deposition of iBTS in toluene solution (0.1 mM) overnight. The terpolymer-nanoparticle composite was prepared by mixing 12 mg of polymer and 6 mg of nanoparticle in toluene/acetone (500/100 μL) and sonicating the mixture for 5 min. The suspension was then applied on the alkylated silicon wafer by drop casting. After air-drying, the coated substrate was irradiated with UV light (254 nm, 7.5 mW cm^{-2}) for 30 min to covalently graft the polymer-nanoparticle composite to the substrate surface using the pendant benzophenone moiety on the polymer.

2.4 Abrasion Test

The robustness of the surface-bound copolymer-nanoparticle coating on the substrate was evaluated by a modified Taber test using eraser rubbing. A pencil (# 2, HB, Ticonderoga) latex free eraser was pressed against the coated substrate mounted to a scale with 300 g force and rubbed back and forth (considered as one rubbing cycle) in a straight line over the surface. After a given amount of rubbing cycles, the damage of the coating was examined by measuring the static contact angle and supercooled water impaction.

2.5 Icing Experiments

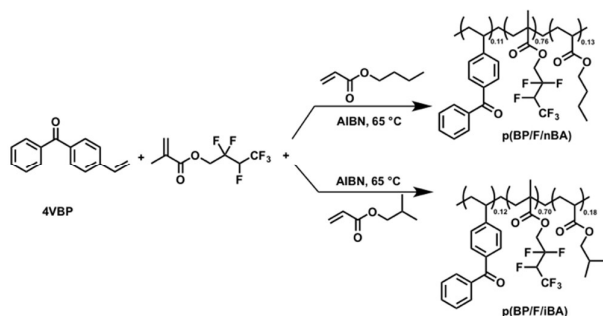
Freezing rain was simulated under a laboratory condition by impinging supercooled water on the samples at subzero temperatures. The preparation of supercooled water, the cold substrate, and decanting water onto the copolymer-nanoparticle coating were conducted in an explosion-proof lab freezer (temperature: -18 °C, relative humidity: 40%). Supercooled water was prepared by carefully cooling still, pure water (18 M Ω) in the freezer for 2 h. Bare and coated substrates were placed in freezer in advance, followed by pouring supercooled water (100 mL) from a 20 cm height. The anti-icing effectiveness of the coating was evaluated by visualizing ice-formation upon impact of supercooled water and recorded by photography and video. The anti-icing capability of the coating was examined before and after abrasion. The icing experiment was repeated 3 times for each sample.

3. Results and discussion

3.1 Cross-linking Kinetics of Terpolymers

The terpolymers, p(BP/F/nBA) and p(BP/F/iBA), which contain benzophenone (BP), hexafluorobutyl (F), and butyl side chains (BA), were prepared by free-radical polymerization of the three

ARTICLE



Scheme 1. Outline of the Synthesis and Chemical Structure of the Terpolymers

monomers (Scheme 1). The terpolymer compositions were checked by NMR spectroscopy, which revealed that the polymer composition matched the pendant group feed ratio (BP : F : BA = 1 : 6 : 1). The hexafluorobutyl side-chain constitutes the majority of the total polymer pendant groups due to hydrophobicity requirement of the polymer. Fluorinated materials possess high hydrophobicity because fluorine has a low polarizability due to its dense electron cloud, which results in weak van der Waals interaction between fluorocarbons and water.⁴⁵ The benzophenone moiety acts as a cross-linker between the polymer and any organic interface through hydrogen abstraction followed by C-C recombination under UV irradiation. Carbon radical stability affects the hydrogen abstraction rate, which further governs the crosslinking kinetics. Previous studies have demonstrated that β -fluorine substitution gives rise to radical destabilization relative to the ethyl radical,⁴⁶ so a more reactive hydrogen is necessary to enhance the cross-linking efficiency. The butyl side-chain was chosen to provide this reactive hydrogen. Two copolymers containing n-butyl and isobutyl acrylate (nBA, iBA) were prepared in order to compare the cross-linking kinetics, mechanical strength, and hydrophobicity between the copolymers with a varying reactivity of abstractable hydrogens.

The cross-linking kinetics of copolymers p(BP/F/nBA) and p(BP/F/iBA) were investigated by UV-vis spectroscopy on an iBTS functionalized quartz substrate. The polymer film was deposited on the alkylated quartz by drop-casting with polymer solution (10 μ L, 10 mg/mL in CHCl_3). Upon absorption of 254 nm light, the promotion of one electron from a nonbonding orbital to the antibonding π^* orbital of the carbonyl group on the BP yields a biradicaloid triplet state where the electron-deficient oxygen n orbital interacts with surrounding weak C-H δ bonds, resulting in H abstraction to complete the half-filled n orbital. The two resulting carbon radicals then combine to form a new C-C bond. This process is monitored by the absorbance decrease in n - π^* transition of BP at 260 nm, as shown in the inset of Fig. 1. The conversion of BP in p(BP/F/iBA) and p(BP/F/nBA) as function of irradiation energy (E, J/cm^2) was determined by plotting the decay of this peak (Fig. 1) at room temperature and elevated temperature. Initial absorbance was normalized to 1 for both polymers. The data can be described by a single-exponential decay:

$$A_{\text{normal}} = e^{-E/E_c} + K \quad (1)$$

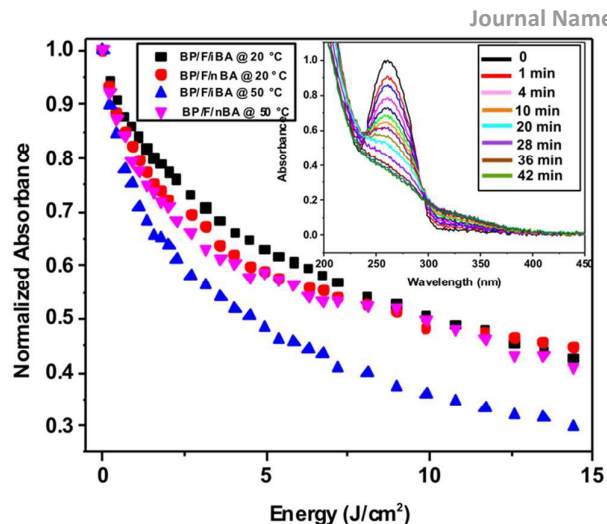


Fig. 1 BP conversion of p(BP/F/iBA) and p(BP/F/nBA) is monitored via UV/vis absorption of the n- π^* peak at 260 nm at experimental temperature of 20 °C and 50 °C. Inset: UV-vis spectra of p(BP/F/iBA) at 20 °C with increasing irradiation time.

where E_c is the characteristic energy for BP conversion and K is the constant absorbance at infinite energy. The decay of the benzophenone triplet is first order,^{47, 48} accordingly the rate constant k is determined as

$$k = \frac{E}{E_c t} \quad (2)$$

where t is the irradiation time. The E_c and k of the two polymers at two different irradiation temperatures are reported in Table 1. Photoinitiation studies have indicated that radical stability of the alkyl pendent group governs the rate of reactivity of BP.⁴⁹ As ketyl radical stability increases with carbon substitution, rate constants for hydrogen abstraction increase in the order of primary, secondary and tertiary. Consequently, iBA is expected to have higher reactivity than nBA due to the tertiary proton. However, when irradiated at room temperature, the E_c of iBA is higher than nBA by 1.8 J/cm^2 . This is likely explained by the segmental motion difference between the two polymer backbones at room temperature. The DSC traces and glass transition temperature (T_g) of two copolymers are given in Fig. S1 and Table 1. Under irradiation, the actual surface temperature of the quartz substrate measured by an infrared thermometer is 31.1 °C. Thus segmental chain movement of p(BP/F/nBA) may occur since the local heating caused by UV irradiation is sufficient to allow the polymer to be raised above its T_g (29.2 °C) during crosslinking. On the other hand, p(BP/F/iBA), with a T_g considerably higher than room temperature (35.4 °C), does not have sufficient free-volume to encounter surrounding C-H groups in the solid state, i.e. hydrogen

Table 1. Irradiation characteristics and glass transition temperatures of the terpolymers used in this study

Copolymer	Irradiation Temp (°C)	E_c (J/cm^2)	k (s^{-1})	T_g (°C)
BP/F/iBA	25 °C	6.4	1.17	35.4
	50 °C	4.0	1.88	
BP/F/nBA	25 °C	4.6	1.63	29.2
	50 °C	4.5	1.67	

abstraction is limited. This assumption is further confirmed by plotting the BP decay and calculating E_c and k at 50 °C, which is well above T_g of both polymers. Under this condition, both polymers have sufficient segmental motion and the reaction rate is governed by the stability of the radical. It should be noted that the difference of E_c and k between two types of butyl side chain is not remarkable (only by 0.5 J cm⁻² and 0.21 s⁻¹, respectively). A plausible explanation is likely that the nBA pendant group contains more 2° hydrogens than iBA. Additionally, although the iBA contains a 3° hydrogen, the reactivity of the 3° C-H is only one order of magnitude higher than 2° C-H. For this reason, the BP cross-linking reaction rate of iBA and nBA are comparable.

The completion of the photochemical cross-linking of the terpolymer was also indicated by GATR-FTIR. Fig. 2 shows the IR spectra of a p(BP/F/iBA) film coated on silicon wafer before and after UV irradiation. In Fig. 2(A) and (B), the ester C-O and C=O stretches are assigned at 1187 and 1746 cm⁻¹. The peak at 1284 cm⁻¹ is due to C-F stretching frequency of the hexafluorobutyl pendant group. The C-C ring vibration is assigned to 1607 cm⁻¹. The peak at 1658 cm⁻¹ in Fig 2(A) represents the C=O stretch of BP chromophore. A significant reduction of this peak, as seen in Fig. 2(B), is a support for the photodegradation of the BP chromophore and formation of the covalent grafting after irradiation.

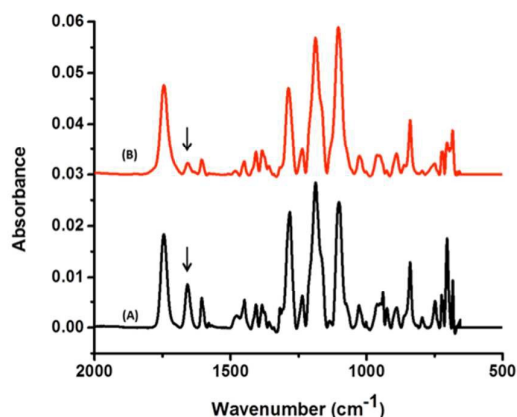
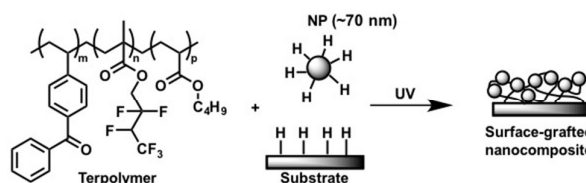


Fig. 2 FTIR spectra of p(BP/F/iBA) film on SiO₂ (A) before and (B) after UV exposure. The peak labeled at 1658 cm⁻¹ is assigned to the C=O stretch of BP chromophore.

3.2 Terpolymer/Nanoparticle Composites

Scheme 2 illustrates the covalent attachment strategy for copolymer/nanoparticle composites to C-H containing surfaces upon UV irradiation. The surface-bound copolymer/surface-alkylated nanoparticle composite was prepared by drop-casting the polymer/NP solvent suspension on alkyl-functionalized silicon wafers and performing photochemical irradiation. In order to obtain a uniform dispersion of the polymer and nanoparticles, the mixture was sonicated vigorously in toluene/acetone co-solvent and then applied to the substrate surface by drop casting. Upon solvent evaporation, the resulting polymer/nanoparticle mixture

remained on the substrate surface with a macroscopically smooth topography. The composite was then irradiated for 45 min to ensure complete BP photo-cross-linking. When the nanoparticles are in the composite, the BP moiety of the copolymer reacts non-selectively with the C-H groups on the silane-treated silicon substrate surface, the nanoparticle surface and the pendent butyl side-chain of polymer itself, resulting in formation of a fluorinated polymeric network embedded with NPs, covalently attached to the substrate surface.



Scheme 2. Covalent attachment of a copolymer/nanoparticle composite to C-H containing substrates.

3.2.1 Surface Morphology

Fig. 3 demonstrates the surface morphology of the UV-cured composite on a silicon substrate. In the SEM images (Fig. 3A), many asperities are seen across the surface, which indicates microscale surface roughness. When magnified (Fig. 3B), the protrusions can be observed to consist of aggregates of nanoparticles, which imply nano-scale roughness. The diameter of the nanospherical feature is ~70 nm based on SEM, which is ~10 nm higher than the average size of the unfunctionalized silica nanoparticle measured by DLS (60 nm, Fig. S2). The micro/nano-scale roughness is also observed by the SEM side view image of the cross section of the composite coated on substrate in Fig 3C. There are numerous nanoparticles embedded in a thin layer of polymer, which are also adhered to the substrate surface. It is noteworthy that in lieu of being completely embedded in a polymer matrix, which would result in a smooth topology, the concentration of nanoparticles is large enough that the nanoscale features of the particles are retained and exposed. Fig. 3D shows the surface profile of the composite coated substrate at the micro-scale (using surface profilometry) with spike-like protrusions and valleys with a width of 25 μm and average roughness of 4.0 μm. Herein, the composite coated substrate shows a surface structure of hierarchical multiscale (micro and nano) roughness. This surface structure directly determines its hydrophobicity and anti-icing capability as discussed below.

3.2.2 Surface Hydrophobicity

The hydrophobicity of the composite coated surface ($m_{\text{polymer}}/m_{\text{NP}} = 2$) is characterized by a static CA and CAH of 138° and 5°, respectively. When a droplet resides on top of a rough surface, two wetting states, the Wenzel state and Cassie-Baxter state, can occur. In the Wenzel state, the droplet impales the grooves and asperities and the contact angle is defined as follows:

$$\cos \theta^* = r_f \cos \theta \quad (3)$$

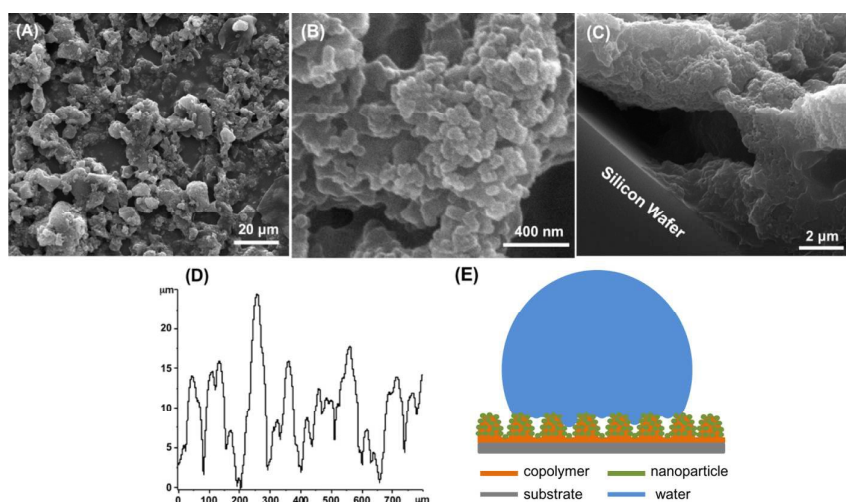


Fig. 3 Morphology study of p(iBP/F/iBA)/nanoparticle composite on alkylated SiO₂ substrates. (A) Representative top view SEM images. (B) Zoom-in SEM image of an asperity. (C) Side view SEM image of coated substrate cross section. (D) Surface profile thickness of the coated surface. (E) Schematic cross-sectional profile of water in contact with a composite coated surface that illustrates the Cassie-Wenzel transition.

where θ^* and θ are the CA on rough and flat surfaces, respectively. r_f , known as the roughness factor, is the ratio of the actual area of the solid surface to the apparent area. In Cassie-Baxter state, the droplet sits on top of the asperities, forming “air pockets” between the liquid and solid surface. In this case, the contact angle is defined by the following equation:

$$\cos \theta^* = f(1 + \cos \theta) - 1 \quad (4)$$

where f is the area fraction of liquid-solid interface. A superhydrophobic surface that consists of hierarchical micro- and nano-scale roughness, combined with a low surface energy moiety, satisfies the Cassie-Baxter model.^{9,50} Based on the surface image and profile shown above, Fig. 3E demonstrates the wetting behavior of the water droplet on these polymer/nanoparticle composites. The composite dual-scale roughness prohibits water droplets to wet the spaces between spikes of both micro- and nanostructure. Consequently, the water-solid contact area is small, due to an extremely small f value ($f_{hierarchical} = f_{micro} \times f_{nano}$). According to Equation 4, the CA of such surface is large. Because of the air entrapment inside the grooved texture, a heterogeneous interface composed of solid and air is generated. As a result, the adhesion force between water and solid is extremely low, which accounts for the observed low hysteresis.

3.2.3 Ice Prevention Towards the Impact of Supercooled Water

One of the methods to examine the anti-icing capability of surfaces involves impacting the tested surface with supercooled water.^{10, 15, 51} In our study, the uncoated and composite coated silicon wafers were tilted at an angle of 5° from horizontal and impinged by a stream of supercooled water. The effectiveness was evaluated by observation of ice generation on the substrate. The videos that recorded the icing experiment in the freezer are provided in Movie S1 and the photos of resulting substrates after ice formation are shown in Fig. 4. In Fig. 4A, the left substrate is the control (bare SiO₂) and the right substrate is the wafer coated with the polymer/particle composite after UV irradiation, where the opaque coating is apparent. On the uncoated substrate, ice

formed instantly when the supercooled water impacted the surface. A full layer of ice is shown on the control whereas no ice was formed on the coated substrate. Only some accumulated water remains on the surface due to the low tilt angle in the experiment. The substrates were warmed back to room temperature and air-dried. The process of striking substrate with supercooled water, warming and drying was considered as one icing/deicing cycle. The icing/deicing process was repeated three times on the same substrate and no ice was formed on the composite coated surface each time. According to previous reports, multiple icing/deicing cycles caused gradual loss of effective icing prevention, as a result of damage of nano-asperities over the expansion of water upon freezing¹³. This is not the case with the crosslinked composite, which has reliable anti-icing capability towards striking of supercooled water after multiple icing/deicing cycles, due to its excellent mechanical durability as described in the following section.

Previous studies have been focused on two aspects to design an anti-icing coating: elimination of ice adhesion and delay or prevention of ice nucleation. It also has been shown that wetting hysteresis directly relates to ice adhesion.¹¹ In this work, the

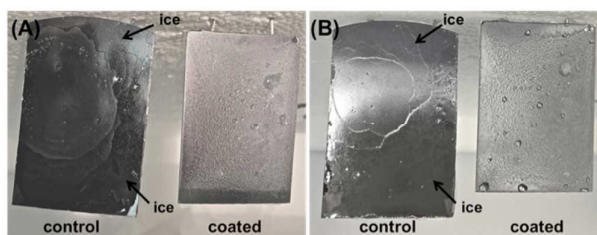


Fig. 4 Optical images demonstrating the anti-icing property of p(BP/F/iBA)/nanoparticle composite coated silicon wafer before (A) and after (B) abrasion.

composite coated surface with a CA of $\sim 140^\circ$ and a CAH of 5° is speculated to be wetted in the Cassie-Wenzel transition state, where water is partially pinned in the grooves or asperities. This mixed state explains the fact that the composite coated surface was slightly wetted after striking with supercooled water (Fig. 4). Thus, instead of reaching a perfectly non-wetting Cassie-Baxter state in which the frozen droplets are easily removed with a small input of thermal energy,¹⁵ the delay of ice nucleation is likely the more important factor that leads to the icephobic nature of this coating. Cao *et al.* systematically investigated the effect of the size of the spherical roughness on icing probability.¹⁰ They successfully demonstrated that the ratio of the free energy barrier between heterogeneous and homogeneous nucleation, f (values between 0 and 1), estimates the anti-icing capability of surfaces with nano-spherical roughness. The mathematic derivation to calculate f and experimental parameters are found in the Supporting Information. Under our experimental conditions of icing, f is plotted versus radius of nanoparticle, R in Fig. 5. f is found to drop dramatically as R increases from 10 to 110 nm. When R is above 1 μm , the size of nanoparticle has little influence on f . This curve implies that within a 10 to 110 nm particle radius, the size of the surface exposed nano-spherical features is the defining parameter in terms of likelihood of preventing ice nucleation. Specifically, the smaller the nanoparticles, the greater the nucleation energy barrier, and lower tendency towards icing on the surface. The radius of our surface exposed nanoparticle is 35 nm based on SEM, and f is 0.862 according to Fig. 5, suggesting a relatively high nucleation free energy barrier. For these reasons, the composite coating has excellent icephobicity towards impinging supercooled water.

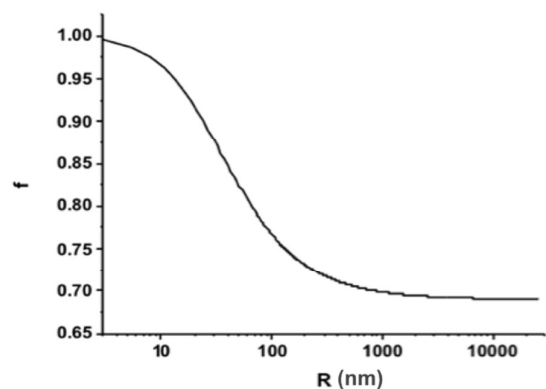


Fig. 5 Relationship of the ratio of free energy barrier between heterogeneous and homogeneous nucleation on spherical surface (f) versus nanoparticle radius (R).

3.2.4 Composites with different polymer/NP ratios

The effect of different terpolymer/nanoparticle composition on morphology and anti-icing capability was also investigated by comparing the composites with a polymer (p(iBP/F/iBA)) nanoparticle mass ratio of 2 and 2.8 (w/w). Fig. 6 illustrates the morphology of the two composites when coated on alkylated SiO_2 substrates. With the composite containing a polymer/nanoparticle ratio of 2 (Fig. 6A), numerous spherical particles are uniformly exposed, which provides nanoscale roughness. However, as the

polymer/nanoparticle composition ratio increases to 2.8 (Fig. 6B), the individual particles start to become buried and submerged in the polymer matrix, which leads to a smoother surface on the nanoscale. The morphology change due to the higher polymer content results in a low CA (122°) and high CAH (22°). The different morphologies of two composites lead to different behavior in icing experiments (Movie S1 and Movie S2). Upon striking of the surface with supercooled water, the composite with polymer/NP ratio of 2 repels the water and prevents icing. In comparison, though inhibiting instant ice formation, the composite with ratio of 2.8 provide much less water repellancy. The remaining water on surfaces can nucleate in sub-zero conditions. Therefore, the proper composition of p(iBP/F/iBA)/NP is essential to enable the optimum amount of nanoscale roughness, which aids in water repellency and icephobicity.

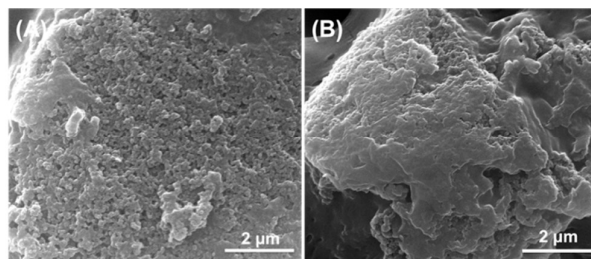


Fig. 6 SEM images of p(iBP/F/iBA)/nanoparticle composites coated on SiO_2 substrates with different polymer/nanoparticle mass ratios. The ratios of polymer/nanoparticle are (A) 2 and (B) 2.8, respectively.

3.3 Robustness of Polymer/Nanoparticle Composites against Abrasion

3.3.1 On Alkylated Glass

The robustness of BP induced covalent bonding to substrate surface was evaluated by conducting an eraser abrasion test (modified Taber testing) on BP containing and non-BP containing polymer/nanoparticle composites. P(BP/F/iBA) was used as the polymer in the tested samples and a homopolymer that only contains the fluorinated hydrocarbon, poly(hexafluorobutyl methacrylate), was used as the control. An eraser with 300 g load was rubbed across the two composite coated samples on silicon substrates 60 times. Optical pictures and water CA of the resultant coating after abrasion testing are shown in Fig. 7. The control poly(hexafluorobutyl methacrylate)/nanoparticle composite

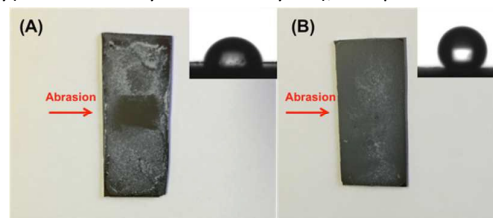


Fig. 7 Abrasion study of polymer/nanoparticle composites coated SiO_2 substrates. Optical images of substrates coated with (A) p(hexafluorobutyl methacrylate) and (B) p(BP/F/iBA)/nanoparticle composite after one cycle of abrasion. Inset: image of water droplet on the substrate.

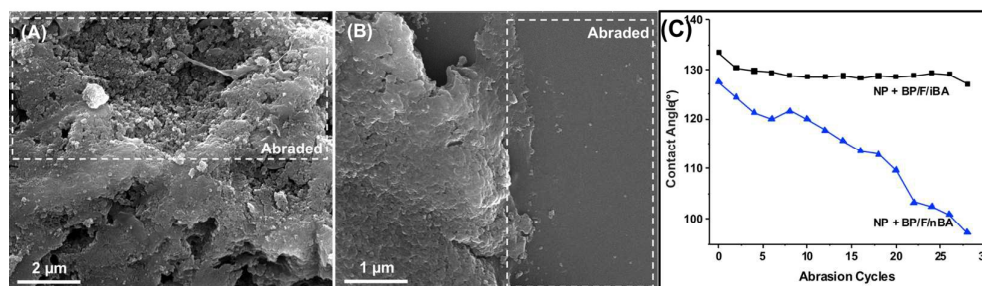


Fig. 8 Robustness of p(BP/F/iBA) and p(BP/F/nBA) nanocomposites against abrasion: SEM images of (A) p(BP/F/iBA) and (B) p(BP/F/nBA) nanocomposites coated SiO₂ surfaces after 28 abrasion cycles (dashed box: abraded area); (C) Plot of mechanical abrasion cycles and static water CA after every other abrasion cycle for p(BP/F/iBA) and p(BP/F/nBA) coated composites.

without BP crosslinker was removed after only one cycle of rubbing, which left the bare substrate with CA of 83°, whereas the BP containing copolymer composite remained, and the surface retained its superhydrophobicity with CA of 140°. This implies that BP moiety can act as a “photo-reactive glue” that combines the polymer and nanoparticles together with adherence to the substrate surface through crosslinking. In comparison, the physisorbed non-BP composite provides no mechanical resistance towards abrasion. Additionally, for the surface-bound composite, as the exterior of the coating is abraded and lost, more deeply embedded nanoparticles are exposed at the interface, and the nano-scale roughness remains intact. Hence, the BP-containing composite presents mechanical resistance to friction. Anti-icing capability of p(BP/F/iBA) nanoparticle composite was tested after 30 abrasion cycles. The video of the icing experiment on the abraded coatings is shown in movie S2 and the resultant substrate is shown in Fig. 4B. No ice formation is observed, demonstrating that the composite not only has excellent anti-icing capability, but also a mechanical robustness that survives harsh abrasion. However, it was observed that some liquid droplets remained on the abraded surface due to the slight decline in surface hydrophobicity (~5° CA decrease after abrasion (Fig. 8(C)).

A comparison of robustness between the terpolymers of p(BP/F/iBA) and p(BP/F/nBA) within the nanoparticle composite was also performed using eraser abrasion testing and subsequent SEM imaging (Fig. 8). The morphology of abraded surfaces coated with p(BP/F/iBA) and p(BP/F/nBA) nanocomposites are presented in Fig. 8A and Fig. 8B, respectively. For p(BP/F/iBA) composite, only the top layer of the nanoparticles was removed after treated with 28 abrasion cycles. The embedded nanoparticles within the polymeric network were exposed and the surface nanoscale roughness was preserved. In contrast, p(BP/F/nBA) nanocomposite was completely removed from the surface after undergoing the same number of abrasion cycles, indicating the adhesive failure of the composite. Furthermore, the CAs were measured over continuous abrasion cycles to characterize the changes of the hydrophobicity for two polymer/nanoparticle composites (Fig. 8C). It was observed that the CA of p(BP/F/nBA) composite drops by ~30° (from 128° to 96°, which is close to the original contact angle of the isobutyl SAM on silicon wafer) after 28 abrasion cycles. On the other hand, the CA of p(BP/F/iBA)

composite decreases by only 5° (from 134° to 129°), retaining its hydrophobicity. The robustness difference is likely explained by the occurrence of β-scission of the polymer backbone during cross-linking. It is suggested that β-scission is one of the pathways a carbon radical can undergo after hydrogen abstraction.⁵² If β-scission occurs on backbone, it causes chain scission in the polymer. For a polyacrylate that contains 3° hydrogens on the polymer backbone, hydrogen abstraction occurs most favorably on the polymer main chain, leading to higher amounts of chain scission and resultant loss in the mechanical integrity of the coating. However, if there are additional 3° hydrogens on the pendent groups (as is the case with an isobutyl side chain), the probability of hydrogen abstraction from the backbone is smaller, where the pendant 3° hydrogens “dilute” the β-scission probability. Additionally, it is likely that isobutyl groups are more accessible for abstraction, and hinder access to the polymer backbone more than *n*-butyl side chains. A similar conclusion was reached by Christensen *et al.* in a recent study on polymer gelation.⁵³

3.3.2 On Plastic

To investigate the versatility of the p(BP/F/iBA)/nanoparticle coating on commercially available plastics, we photochemically modified a polypropylene (PP) sheet with the composite by drop-casting using the same material composition described above. The PP substrates were irradiated to covalently graft the copolymer/nanoparticle to the plastic surface via hydrogen abstraction from the PP surface. After UV curing, the uncoated and coated PP substrates were challenged against the icing test using the icing experimental method described above. Fig. 9 shows the anti-icing capability of composite coated PP before (A) and after (B) eraser abrasion (300 g, 30 cycles). In both (A) and (B), ice is observed on the pristine PP substrate (left). No ice formation occurred on the composite coated PP substrate (right) before and after undergoing 30 abrasion cycles. These results demonstrate that the covalent immobilization of durable

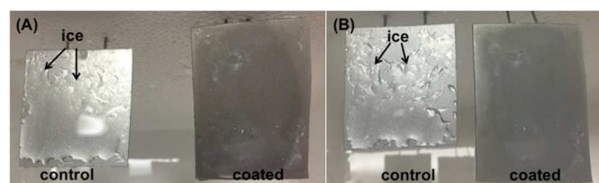


Fig. 9 Optical images demonstrating the anti-icing property of a p(BP/F/iBA)/nanoparticle composite coated polypropylene substrate before (A) and after (B) abrasion.

copolymer/nanoparticle composite is applicable to a variety of substrates, including inert plastics.

4. Conclusions

In conclusion, we have demonstrated an efficient and easy-to-implement approach to covalently attach an anti-icing composite on to any plastic substrate or surface that contains C-H bonds. The copolymer contains pendant benzophenone, hexafluorobutyl, and isobutyl side chains. When the polymer is combined with silica nanoparticles, a composite that consists of a densely cross-linked network is immobilized on a substrate surface via covalent bonds upon UV irradiation. The optimized copolymer/nanoparticle composite exhibits fast attachment and good mechanical durability when subjected to abrasion. No ice formation occurred on the coated surface when subjected to supercooled water for both abraded and non-abraded coatings. This simple, one step photochemical attachment of icephobic coatings is promising and scalable for domestic and industrial applications. In addition, we have observed that incorporation of 3° hydrogens on pendent groups of BP containing polymer reduces the backbone chain scission occurrence and improves the overall crosslinking possibility and mechanical strength of the coatings after irradiation. This study provides some design principles for polymer/nanoparticle composites that have excellent anti-icing capability along with robust attachment and mechanical durability.

Acknowledgements

The authors gratefully acknowledge financial support from Georgia Research Alliance and the GRA Ventures Program.

References

- J. L. Laforte, M. A. Allaire and J. Laflamme, *Atmos. Res.*, 1998, **46**, 143-158.
- Y. Shen, J. Tao, H. Tao, S. Chen, L. Pan and T. Wang, *Langmuir*, 2015, DOI: 10.1021/acs.langmuir.5b02946.
- L. O. Andersson, C. G. Golander and S. Persson, *J. Adhes. Sci. Technol.*, 1994, **8**, 117-132.
- R. W. Gent, N. P. Dart and J. T. Cansdale, *Phil. Trans. R. Soc. Lond.*, 2000, **358**, 2873-2911.
- V. K. Croutch and R. A. Hartley, *J. Coat. Technol.*, 1992, **64**, 41-53.
- S. Jung, M. K. Tiwari, N. V. Doan and D. Poulidakos, *Nat Commun*, 2012, **3**, 615.
- K. K. Varanasi, T. Deng, J. D. Smith, M. Hsu and N. Bhate, *Appl. Phys. Lett.*, 2010, **97**, 234102.
- K. K. Varanasi, M. Hsu, N. Bhate, W. Yang and T. Deng, *Appl. Phys. Lett.*, 2009, **95**, 094101.
- J. Xiao and S. Chaudhuri, *Langmuir*, 2012, **28**, 4434-4446.
- L. Cao, A. K. Jones, V. K. Sikka, J. Wu and D. Gao, *Langmuir*, 2009, **25**, 12444-12448.
- S. A. Kulinich and M. Farzaneh, *Langmuir*, 2009, **25**, 8854-8856.
- S. A. Kulinich and M. Farzaneh, *Appl. Surf. Sci.*, 2009, **255**, 8153-8157.
- S. A. Kulinich and M. Farzaneh, *Cold Reg. Sci. Technol.*, 2011, **65**, 60-64.
- A. J. Meuler, J. D. Smith, K. K. Varanasi, J. M. Mabry, G. H. McKinley and R. E. Cohen, *ACS Appl. Mater. Interfaces*, 2010, **2**, 3100-3110.
- L. Mishchenko, B. Hatton, V. Bahadur, J. A. Taylor, T. Krupenkin and J. Aizenberg, *ACS Nano*, 2010, **4**, 7699-7707.
- P. Tourkine, M. Le Merrer and D. Quéré, *Langmuir*, 2009, **25**, 7214-7216.
- H. Saito, K. Takai and G. Yamauchi, *Surf. Coat. Int.*, 1997, **80**, 168-171.
- S. A. Kulinich and M. Farzaneh, *Vacuum*, 2005, **79**, 255-264.
- R. Menini, Z. Ghalimi and M. Farzaneh, *Cold Reg. Sci. Technol.*, 2011, **65**, 65-69.
- S. Farhadi, M. Farzaneh and S. A. Kulinich, *Appl. Surf. Sci.*, 2011, **257**, 6264-6269.
- X. Deng, L. Mammen, Y. Zhao, P. Lellig, K. Müllen, C. Li, H.-J. Butt and D. Vollmer, *Adv. Mater.*, 2011, **23**, 2962-2965.
- P. M. Hansson, L. Skedung, P. M. Claesson, A. Swerin, J. Schoelkopf, P. A. C. Gane, M. W. Rutland and E. Thormann, *Langmuir*, 2011, **27**, 8153-8159.
- N. J. Turro, *Modern Molecular Photochemistry*, Benjamin/Cummings Pub. Co.: Menlo Park CA., 1978.
- A. A. Lin, V. R. Sastri, G. Tesoro, A. Reiser and R. Eachus, *Macromolecules*, 1988, **21**, 1165-1169.
- M.-K. Park, S. Deng and R. C. Advincula, *J. Am. Chem. Soc.*, 2004, **126**, 13723-13731.
- H. Higuchi, T. Yamashita, K. Horie and I. Mita, *Chem. Mater.*, 1991, **3**, 188-194.
- C. Braeuchle, D. M. Burland and G. C. Bjorklund, *J. Phys. Chem.*, 1981, **85**, 123-127.
- J. Pahnke and J. Rühle, *Macromol. Rapid Commun.*, 2004, **25**, 1396-1401.
- O. Prucker, C. A. Naumann, J. Rühle, W. Knoll and C. W. Frank, *J. Am. Chem. Soc.*, 1999, **121**, 8766-8770.
- V. P. Dhende, S. Samanta, D. M. Jones, I. R. Hardin and J. Locklin, *ACS Appl. Mater. Interfaces*, 2011, **3**, 2830-2837.
- K. Horie, K. Morishita and I. Mita, *Macromolecules*, 1984, **17**, 1746-1750.
- K. Horie, H. Ando and I. Mita, *Macromolecules*, 1987, **20**, 54-58.
- J. Yatvin, S. A. Sherman, S. F. Filocamo and J. Locklin, *Polym. Chem.*, 2015, **6**, 3090-3097.
- R. Navarro, M. Pérez Perrino, O. Prucker and J. Rühle, *Langmuir*, 2013, **29**, 10932-10939.
- L.-H. Liu and M. Yan, *Acc. Chem. Res.*, 2010, **43**, 1434-1443.
- A. Blencowe and W. Hayes, *Soft Matter*, 2005, **1**, 178-205.
- G. Dorman and G. D. Prestwich, *Biochemistry*, 1994, **33**, 5661-5673.
- J. D. J. S. Samuel, T. Brenner, O. Prucker, M. Grumann, J. Ducree, R. Zengerle and J. Ruehe, *Macromol. Chem. Phys.*, 2010, **211**, 195-203.
- S. Hu, X. Ren, M. Bachman, C. E. Sims, G. P. Li and N. L. Allbritton, *Anal. Chem.*, 2004, **76**, 1865-1870.
- K. Abu-Rabeah, D. Atias, S. Herrmann, J. Frenkel, D. Tavor, S. Cosnier and R. S. Marks, *Langmuir*, 2009, **25**, 10384-10389.
- T. Brandstetter, S. Boehmer, O. Prucker, E. Bisse, A. zur Hausen, J. Alt-Moerbe and J. Ruehe, *J Virol Methods*, 2010, **163**, 40-48.
- J. Kim, J. A. Hanna, M. Byun, C. D. Santangelo and R. C. Hayward, *Science*, 2012, **335**, 1201-1205.
- J. Kim, J. A. Hanna, R. C. Hayward and C. D. Santangelo, *Soft Matter*, 2012, **8**, 2375-2381.

ARTICLE

Journal Name

- 44 A. Virkar, M.-M. Ling, J. Locklin and Z. Bao, *Synth. Met.*, 2008, **158**, 958-963.
- 45 X. Li, J. Li, M. Eleftheriou and R. Zhou, *J. Am. Chem. Soc.*, 2006, **128**, 12439-12447.
- 46 W. R. Dolbier, *Chem. Rev.*, 1996, **96**, 1557-1584.
- 47 J. C. Scaiano, E. B. Abuin and L. C. Stewart, *J. Am. Chem. Soc.*, 1982, **104**, 5673-5679.
- 48 J. A. Bell and H. Linschitz, *J. Am. Chem. Soc.*, 1963, **85**, 528-533.
- 49 M. R. Topp, *Chem. Phys. Lett.*, 1975, **32**, 144-149.
- 50 E. Huovinen, J. Hirvi, M. Suvanto and T. A. Pakkanen, *Langmuir*, 2012, **28**, 14747-14755.
- 51 Y. Wang, J. Xue, Q. Wang, Q. Chen and J. Ding, *ACS Appl. Mater. Interfaces*, 2013, **5**, 3370-3381.
- 52 A. Torikai, Y. Sekigawa and K. Fueki, *Polym. Degrad. Stab.*, 1988, **21**, 43-54.
- 53 S. K. Christensen, M. C. Chiappelli and R. C. Hayward, *Macromolecules*, 2012, **45**, 5237-5246.

Journal Name

ARTICLE

Journal of Materials Chemistry A Accepted Manuscript

Published on 05 July 2016. Downloaded by LA TROBE UNIVERSITY on 05/07/2016 14:47:16.